Fast two-photon *in vivo* imaging with three-dimensional random-access scanning in large tissue volumes

Gergely Katona[1,5], Gergely Szalay[1,5], Pál Maák[2,5], Attila Kaszás[1,3,5], Máté Veress[2], Dániel Hillier[4], Balázs Chiovini[1], E Sylvester Vizi[1], Botond Roska[4] & Balázs Rózsa[1,3]

The understanding of brain computations requires methods that read out neural activity on different spatial and temporal scales. Following signal propagation and integration across a neuron and recording the concerted activity of hundreds of neurons pose distinct challenges, and the design of imaging systems has been mostly focused on tackling one of the two operations. We developed a high-resolution, acousto-optic two-photon microscope with continuous three-dimensional (3D) trajectory and random-access scanning modes that reaches near-cubic-millimeter scan range and can be adapted to imaging different spatial scales. We performed 3D calcium imaging of action potential backpropagation and dendritic spike forward propagation at sub-millisecond temporal resolution in mouse brain slices. We also performed volumetric random-access scanning calcium imaging of spontaneous and visual stimulation–evoked activity in hundreds of neurons of the mouse visual cortex *in vivo*. These experiments demonstrate the subcellular and network-scale imaging capabilities of our system.

The systematic understanding of brain function requires methods that allow recording neuronal activity at different spatial scales in three dimensions at high temporal resolution. In single neurons, activity is differently distributed in space and time across the dendritic and axonal segments[1–6]. Therefore, to understand neuronal-signal integration, activity should be simultaneously recorded at many spatial locations in the dendritic and axonal tree of a single neuron[2]. In neuronal circuits, closely spaced neurons can have vastly different activity patterns[7]; in contrast, widely separated cells may belong to the same functional circuit, influencing each other via long axonal processes. Therefore, recording techniques are required that collect information near-simultaneously (in one fast measurement sequence) from many cells of a neuronal population situated in an extensive volume of tissue. Moreover, measurements should be possible on the timescale of the dendritic integration of signals, of the transformation of incoming signals

to neuronal output and of the propagation of spikes[8], that is, with sub-millisecond temporal resolution.

Several technologies have been developed to achieve fast 3D measurements from brain tissue, including fast liquid lenses, deformable mirrors, temporal and spatial multiplexing[9,10], axicon or planar illumination-based imaging[11], holographic scanning[12], and piezo-scanning with sinusoidal and nonlinear resonance[2,13]. Acousto-optic (AO) scanning technology has also been used to rapidly change beam focusing without mechanical movement[14], and AO technology for two-photon microscopy has been adapted in several applications[14–24]. However, there are limitations in the use of these methods for 3D optical recordings both *in vitro* and *in vivo*. In *in vitro* applications, new 3D technologies either have not yet been validated in functional measurements on biological samples[10,14,19,21,22], or they do not simultaneously fulfill technical criteria that are necessary to follow backpropagation of action potentials or Ca^{2+} spikes in dendrites, which often extend over hundreds of micrometers[2,7,9–25]. Regarding *in vivo* applications, random-access recording of the activity of hundreds of selected neurons has not been validated *in vivo* in three dimensions[17].

We developed a two-photon 3D laser-scanning microscope with a millimeter *z*-dimension scanning range and sub-millisecond temporal resolution. We demonstrated its use for single-neuron imaging *in vitro* by obtaining 3D optical recordings of action potential backpropagation at sub-millisecond temporal resolution with random-access scanning as well as dendritic Ca^{2+} spike forward propagation in several-hundred-micrometer-long neuronal processes with the continuous 3D trajectory scanning mode. We demonstrated the use of the microscope for imaging neuronal populations *in vivo* by 3D random-access scanning of Ca^{2+} transients in hundreds of neurons in the mouse visual cortex at 80 Hz.

RESULTS
The 3D-imaging microscope design
We used a detailed optical model to find combinations of all active and passive optical elements in the scanning light path of

the microscope that would provide the maximal exploitation of the apertures of all lenses in the 20× objective (numerical aperture (NA) = 0.95) at different x, y and z scanning positions and therefore result in the smallest point spread function (PSF) in the largest possible scanning volume (**Fig. 1a**, **Supplementary Fig. 1**, **Supplementary Note 1** and **Online Methods**). The resulting system contains new design concepts: it physically separates the z-dimension focusing and lateral scanning functions to optimize the lateral AO scanning range (**Fig. 1a,b** and **Supplementary Fig. 2**); it allows the acoustic frequency chirps in the deflectors to be adjusted dynamically to compensate for astigmatism and optical errors (**Fig. 1a,c** and **Supplementary Fig. 3**); it involves a custom angular compensation unit to diminish off-axis angular dispersion introduced by the AO deflectors (**Fig. 1a–c**, **Supplementary Fig. 3d,e** and **Supplementary Note 2**); and it uses a high-NA, wide-field objective and high-bandwidth custom AO deflectors with large apertures (17 mm and 15 mm; **Supplementary Note 3**) to obtain 0.47–1.90 μm lateral and 2.49–7.9 μm axial PSF sizes, short pulse duration in a 700 μm × 700 μm × 1,400 μm (x, y and z) volume (**Fig. 1a–e**, **Supplementary Figs. 2c**, **3a,b** and **4–7**,

Supplementary Note 4 and **Supplementary Results 1**). In this large 3D scanning volume, the PSF was smaller than the average size of neuronal somata and neuronal cell bodies can therefore be resolved. In a 290 μm × 290 μm × 200 μm core volume, the lateral and axial PSFs remained below 0.8 μm and 3 μm, respectively, and the device therefore could resolve dendrites. Temporal stability was ensured by a beam stabilization unit and by active cooling of the acousto-optics. We maximized two-photon excitation efficiency by ensuring minimum pulse length, using the combination of a fixed four-prism and an adjustable two-prism compressor. In 3D random-access scanning mode, 2–2,000 points were scanned near-simultaneously, in one measurement cycle, with 23.8/N kHz to 54.3/N kHz, where N denotes the number of points (**Fig. 1f**). Details of the microscope design are available in **Online Methods** and **Supplementary Note 1**.

3D random-access scanning of action-potential propagation

We examined the temporal resolution of our system by imaging propagating activity at 87 3D locations of a single hippocampal neuron in acute hippocampal mouse brain slices.
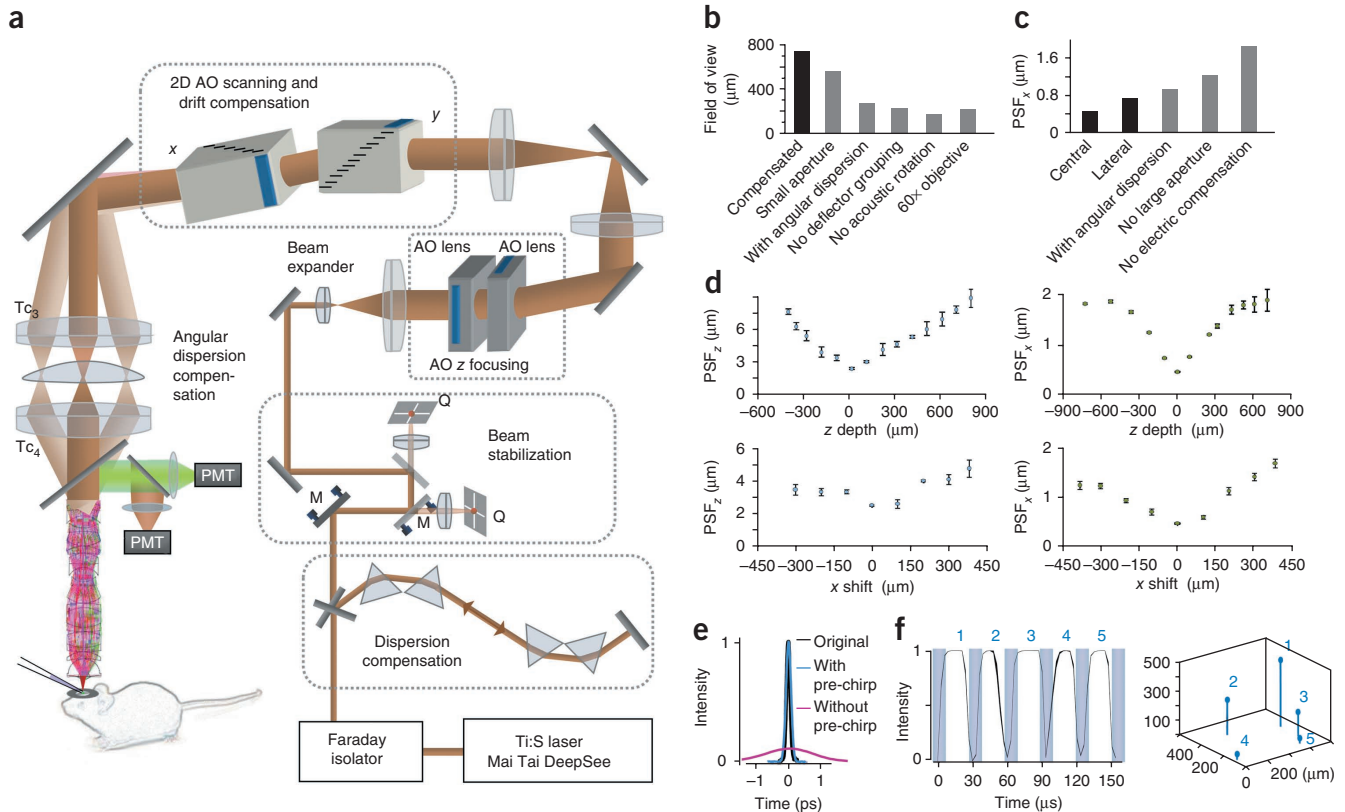

Figure 1 | Design and characterization of the two-photon microscope setup. (**a**) Schematics of microscope setup. Material-dispersion compensation was adjusted with a four prism compressor and a Ti:S laser. A Faraday isolator eliminated coherent back reflections. Motorized mirrors (M) stabilized the position of the beam on the surface of two quadrant detectors (Q) before the beam expander. Two AO deflectors optimized for diffraction efficiency controlled the z focusing of the beam (AO z focusing). A 2D AO scanner unit (2D-AO scanning) performed x-y scanning and drift compensation during z scanning. A spherical field lens in the second telecentric lens system (Tc$_3$ and Tc$_4$) provided additional angular dispersion compensation. PMT, photomultiplier tubes. (**b**) The maximal field of view (compensated, black bar) is shown when both deflector pairs were used for deflection (no deflector grouping) or when optically rotated deflectors (no acoustic rotation), small aperture objectives (60× objective), no angular dispersion compensation (with angular dispersion) or small aperture acousto-optic deflectors were used (small aperture). (**c**) The compensated PSF size along x axis (PSF$_x$) (central, black bar) at (x, y, z) = (150, 150, 100) μm coordinates (lateral) or when no angular dispersion compensation (with angular dispersion), no electronic compensation (no electric compensation) or reduced AO apertures were applied (no large apertures). (**d**) PSF$_z$ and PSF$_x$ variation as a function of z depth and lateral AO scanning (x shift). Error bars are mean ± s.d., n = 5. (**e**) Temporal width of the laser pulse at the laser output (original), and before the objective lens with and without dispersion compensation (prechirp). (**f**) Five fluorescent beads (diameter 6 μm; locations, blue points) were repetitively scanned in random-access mode in an 800 μm × 600 μm × 500 μm sample. Image shows bead locations (right). Five overlaid fluorescence measurements are shown (left).

Figure 2 | Three-dimensional measurement of BAPs with sub-millisecond resolution. (**a**) A 3D view of the dendritic arbor of a CA1 pyramidal cell imaged with 3D AO scanning (top, z stack); spheres represent the measurement locations. Maximum intensity z-projection image of the same neuron (bottom left); recorded dendrites are numbered. Schema of the apical trunk and the dendritic branches of the neuron (bottom right) showing calcium transients recorded near-simultaneously in each of the dendrites, averaged from five traces. Scale bars, 100 μm. (**b**) Dendritic Ca^{2+} transients measured from the same dendritic point of the apical trunk (average of five traces) and corresponding somatic voltage traces (V_m). (**c**) Experimental arrangement for signal propagation experiments. Signal propagation speed was measured by somatic whole-cell current-clamp (V_m, black), cell-attached current-clamp (cyan, purple) and 3D two-photon calcium imaging (orange, pink, green and blue). The same color-coding is used in **c–g**. (**d**) Triggered action potential peak and averaged and normalized backpropagating calcium transients (mean ± s.e.m.; n = 54; top). Linear fits (red dashed lines) define onset latency times. Maximal temporal resolution achieved: 39 μs (SEM_T, x-axis projection of s.e.m., inset). Cell-attached somatic voltage recording (cyan) peaked at the maximum of the derivate ($\delta V_m / \delta t$) of V_m (brown trace; bottom). Somatic (orange) versus dendritic (green) Ca^{2+} transients and position-matched cell-attached signals (dendritic, magenta; somatic, cyan). Arrows point to the lag of the Ca^{2+} signals. (**e**) Transients in **d** in extended time scale. (**f**) First derivatives of the Ca^{2+} transients shown in **d**. (**g**) Onset latency times (mean ± s.e.m., n = 54) of Ca^{2+} transients in **d** as a function of dendritic distance. Linear fit: average propagation speed. (**h**) Dendritic propagation speeds at different temperatures (mean ± s.e.m., n = 5 cells).
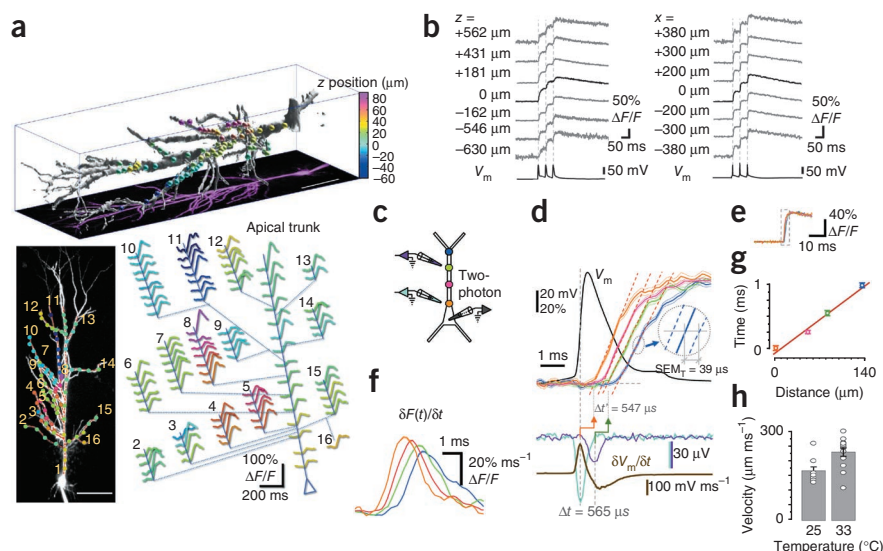
We patch-clamped CA1 pyramidal cells in whole-cell mode and filled the cells with the green fluorescent Ca^{2+} sensor Fluo-5F and the red fluorescent marker Alexa Fluor 594. We positioned the objective at a depth such that the center of the region of interest was in focus, fixed the objective at this position and acquired a reference z-dimension stack (z stack) of images using 3D AO scanning only. The imaged subvolume containing the cell was 700 μm × 700 μm × 140 μm (x, y and z) (**Fig. 2a**). We selected points along the dendritic tree of one neuron from the z stack using either a 3D virtual environment (**Supplementary Video 1** and **Supplementary Note 5**) or by scrolling through the z stack in a 2D virtual environment[2]. We held the cell in current-clamp mode and evoked an action potential by somatic current injection while near-simultaneously measuring dendritic Ca^{2+} signals associated with the backpropagating action potential (BAP) by repetitively scanning the selected 3D coordinates at 29.76 kHz (**Fig. 2a** and **Supplementary Fig. 8a,b**). When sample drift occurred, we repositioned single or grouped points manually or automatically (see below). As the acute brain slices were 300 μm thick, we used only a fraction of the total AO z-scanning range. To test whether our random-access 3D AO scanning can be used to record BAP-induced Ca^{2+} transients, we moved the objective focal plane mechanically from +562 μm to −630 μm away from the z center, then used AO z focusing to refocus the recorded dendritic tree (**Fig. 2b**). Independent of the AO z settings, single BAPs could be resolved in Ca^{2+} transients induced by a train of three action potentials (**Fig. 2b** and **Supplementary Fig. 8c–e**). Similarly, single BAPs could be followed in a 760-μm lateral scanning range (**Fig. 2b** and **Supplementary Fig. 8d,e**). We extended the AO z-setting range in which single action potentials could be resolved over 2,000 μm using a 16× objective (**Supplementary Fig. 8f**). In summary, resolution of single action potential–induced transients was possible in a near-cubic-millimeter scanning volume.

We additionally tested the temporal resolution of the microscope by measuring the propagation speed of BAPs. Similarly to above, we evoked a somatic action potential in a pyramidal cell held under current clamp while scanning in 3D along its dendrite. We correlated extracellular cell-attached electric recordings with the acquired optical recordings of the matching dendritic locations (**Fig. 2c**). The BAP-evoked Ca^{2+} transients showed increasing latency in dendritic measurements taken farther away from the cell body (**Fig. 2d,e**). The peak of the extracellular voltage signal was coincident with the peak of the first derivative of the current-clamp signal at the soma (**Fig. 2d**). The temporal delays between the onset of somatic versus dendritic Ca^{2+} transients ($\Delta t'$; **Fig. 2d**) were similar to the delays measured by extracellular recording (Δt) in the same locations (t-test, P > 0.3, n = 5 cells), validating the optical measurements. We could also follow the BAP by detecting the peak of the first derivative of the Ca^{2+} transients at different spatial positions (**Fig. 2f**). We calculated the velocity of the BAP from the latency of the Ca^{2+} transients and the distance from the soma (**Fig. 2g**). Average BAP propagation speed was different at 23 °C and 33 °C (164 ± 13 μm ms^{-1} (n = 9) versus 227 ± 14 μm ms^{-1} (n = 13); P = 0.006, t-test, **Fig. 2h**).

We then asked whether the temporal resolution of the system would allow the investigation of rapid action potential backpropagation at a spatial resolution of a few micrometers. This spatial dimension allows discriminating the activity of small adjacent dendritic segments that *in vivo* act as computational subunits and have an important role in integrating information in a dendrite[2,26,27]. Here we defined the temporal resolution as the smallest significantly (P < 0.05) resolvable x-axis delay between two BAP-induced Ca^{2+} transients occurring during the rising period, when we measured the transients sequentially in two different dendritic locations (**Supplementary Fig. 9**). According to our theoretical predictions (**Supplementary Note 6**, equations

Figure 3 | Point-by-point and continuous 3D trajectory scanning of dendritic Ca^{2+} spike propagation in CA1 pyramidal cells. (**a**) Maximum-intensity projection AO image of a CA1 pyramidal cell. Ca^{2+} transients in dendritic spines (orange and magenta traces) after induction of dendritic Ca^{2+} spike by focal extracellular stimulation (electrode, yellow). Enlarged views are shown in insets. Purple dots represent scanning points in a dendrite. (**b**) Spatially normalized and projected Ca^{2+} signals in the purple dotted dendritic region in **a** (average of five subthreshold responses). Black dashed line, stimulus onset. Column labeled 'S', somatic Ca^{2+} response. (**c**) Ca^{2+} transients derived from the color-coded and numbered regions indicated in **b**. Baseline-shifted Ca^{2+} transients measured in the region contained in the dashed box in **a** (right). Yellow dots, onset latency times at the half-maximum. (**d**) Onset latency times at the peak of the derivate ($\delta F(t)/\delta t$) of Ca^{2+} transients shown in **c**. (**e**) Onset latency times as a function of dendritic distance from the soma for somatic subthreshold (d-spike, black) and suprathreshold (d-spike+AP, blue) dendritic Ca^{2+} spikes. (**f**) Point-by-point and continuous 3D trajectory scanning of dendritic segments. Schema of the scanning modes (top right; blue, point-by-point scanning; green, continuous scanning). Example of Ca^{2+} responses measured by point-by-point (top left) and continuous trajectory modes (bottom). Traces were spatially normalized. (**g**) Image of a fluorescent bead in continuous trajectory scanning mode. The bead image was elongated because the focal spot was moving during PMT integration. Scale bar, 2 μm.

23 and 24), for the highest temporal resolution measurements could be performed in two points situated as close as 6–14 μm in the main apical tuft of CA1 pyramidal cells (**Supplementary Results 2** and **Supplementary Fig. 9c**). The best temporal resolution attained when two transients remained significantly different ($P < 0.05$, t-test) in a temporal interval during the rising phase was 54.7 μs (**Supplementary Fig. 9d**). In addition to measurements of temporal latency, our measurements could also be used to reconstruct the mean time course of transients by adopting a 'random equivalent-time sampling mode' based on oscilloscope technology[28] (Online Methods and **Supplementary Fig. 10**). The 54.7 μs temporal resolution demonstrated here allowed the measurement of fast regenerative activity at the scale of small dendritic segments.

3D trajectory scanning of dendritic spike propagation

Given the importance for neuronal information processing of integrating the activity taking place in the dendrites[1,3,4] as well as the action potential propagation along the axon[29], methods to measure Ca^{2+} levels at many spatial locations in long neuronal processes are required. Here we show two different ways of scanning neuronal processes along 3D trajectories.

First we adapted random-access scanning to measure activity at many discrete points along the 3D trajectory of a dendrite (point-by-point trajectory scanning). As above, we scrolled through a reference z stack of prerecorded images and selected guide points along the length of a dendrite. Then, instead of recording from these manually selected points, we homogeneously resampled the trajectory using interpolation[2] (Online Methods). The speed of the measurement depended on the number of recording points along the trajectory. In the example shown in **Figure 3**, we filled a hippocampal CA1 pyramidal cell with the fluorescent calcium indicator Fluo-5F, pentapotassium salt (Fluo-5F) and induced dendritic Ca^{2+} spikes by focal synaptic stimulation with an extracellular electrode at a distance of >400 μm from the cell body (Online Methods and **Supplementary Protocol 1**). We followed the propagating activity optically at uniformly spaced locations along a dendrite (**Fig. 3a**). We normalized the recorded traces by calculating ($\Delta F/F$; Online Methods, equation (4)) at each point and projected them as a function
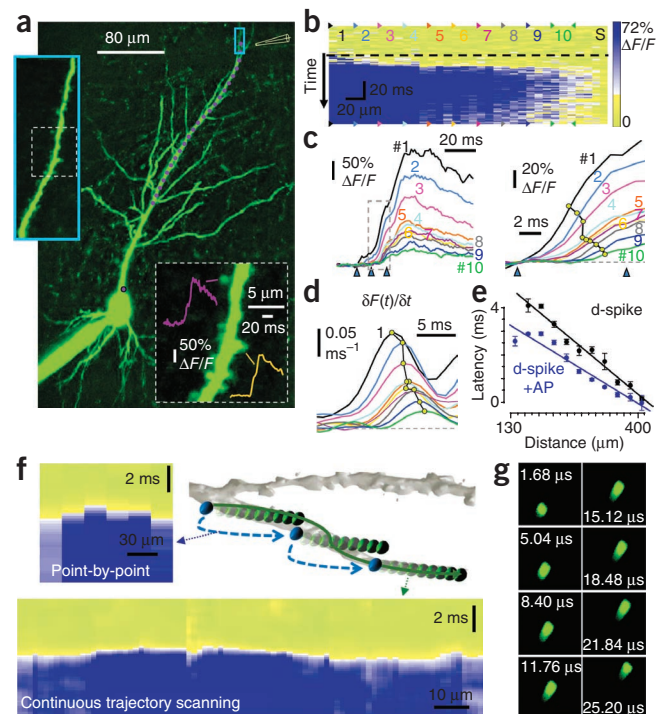
of time and distance measured along the 3D trajectory line (3D Ca^{2+} responses; Online Methods and **Fig. 3b**). The Fluo-5F responses revealed dendritic spikes propagating toward the cell body, both when the stimulation evoked somatic action potentials (suprathreshold spikes) and when the stimulation was insufficient to evoke somatic action potentials (subthreshold spikes) (**Fig. 3b–e**). After a short initiation phase, subthreshold dendritic spikes propagated rapidly and then gradually ceased before reaching the cell body (**Fig. 3b**). We quantified spike propagation speed by measuring propagation times at the half-maximal amplitude of the transients or at the peak of their first derivates (**Fig. 3c,d**). The average propagation speed was significantly higher (131%, t-test, $P = 0.03$, $n = 7$) for suprathreshold spikes than for subthreshold spikes (subthreshold, 81 ± 27 μm ms^{-1} and suprathreshold, 129 ± 30 μm ms^{-1}), and both supra- and subthreshold spikes propagated in the direction of the cell body under these conditions (**Fig. 3e**). Despite the large scanning volume (290 μm × 290 μm × 200 μm), two-photon resolution was preserved (0.47–0.75 μm).

A limitation of the point-by-point trajectory scanning along long dendritic processes is the relatively long switching time (~10–20 μs) between two selected dendritic points. This is a consequence of the long traveling time of the acoustic waves across the large apertures (15–17 mm) of the AO deflectors, required to achieve high spatial resolution in large scanning volumes. Therefore, in this system, we limited the total number of measured points along a given trajectory to 23.8–54.3 points per kHz.

To achieve both high temporal and spatial sampling rates, we adopted a second approach named the 'continuous trajectory scanning' approach based on the 'roller coaster scanning' method[2] that we originally developed for mirror-based scanners. Both of these methods have similar spatial discrimination, but the fast z-scanning range of continuous trajectory scanning is not limited to ~20 μm and can be hundreds of micrometers. Moreover, mechanical constraints do not limit trajectory selection.
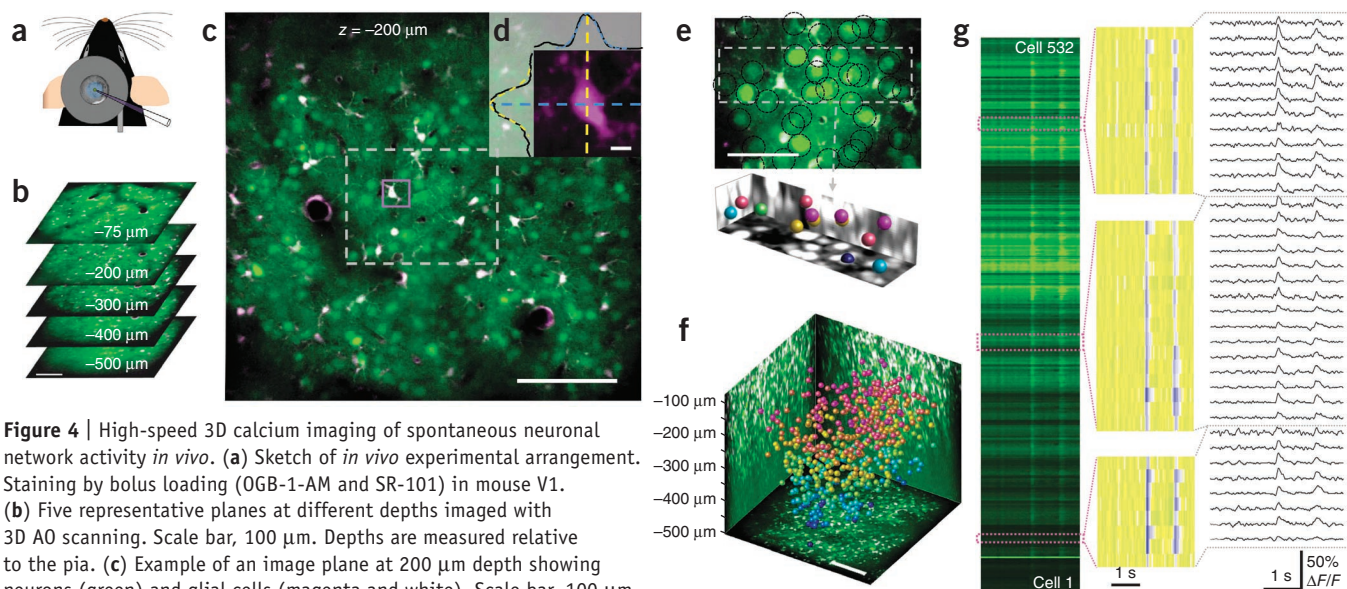
Figure 4 | High-speed 3D calcium imaging of spontaneous neuronal network activity *in vivo*. (**a**) Sketch of *in vivo* experimental arrangement. Staining by bolus loading (OGB-1-AM and SR-101) in mouse V1. (**b**) Five representative planes at different depths imaged with 3D AO scanning. Scale bar, 100 μm. Depths are measured relative to the pia. (**c**) Example of an image plane at 200 μm depth showing neurons (green) and glial cells (magenta and white). Scale bar, 100 μm. (**d**) Image and intensity profiles of a pre-selected bright glial cell (purple box in **c**) used to establish the coordinate system. Scale bar, 5 μm. (**e**) A 35 μm *z*-projection of the dashed boxed region marked in **c** (top). Neuronal somata detected with the aid of an algorithm in a subvolume (shown with projections, neurons in white and glial cells in black; bottom). Scale bar, 50 μm. (**f**) Maximal intensity side and *z* projections of the entire *z* stack (400 μm × 400 μm × 500 μm) with autodetected cell locations (spheres) color-coded in relation to depth following the legend in **Figure 2a**. The set detection threshold yields 532 neurons. Scale bar, 100 μm. (**g**) Spontaneous neuronal network activity measured in the 532 cells in **f**. Example of a raw trace in which each line corresponds to a cell (left). Spatially normalized traces (middle) and corresponding Ca²⁺ transients (right).

To implement the continuous trajectory scanning approach, we first selected guide points in three dimensions along a neuronal process and calculated an interpolation curve as above. Then we focused the laser on the first guide point, where the interpolation curve starts. Next, we forced the focal point to drift continuously in the *x-y* plane in the direction of the interpolation curve (Online Methods and **Supplementary Note 7**) until the distance between the center of the focal point and the interpolation curve exceeded 50% of the size of the PSF in the *z* direction (**Fig. 3f,g** and **Supplementary Fig. 1d**). Then we stepped the focal spot along the *z* axis, in the direction of the interpolation curve, with a step size corresponding to the PSF size. From this new position, we restarted the drift-jump procedure and repeated it until the end of the interpolation curve was reached (corresponding to the last guide point). We determined the required drift velocity by equation (2) in Online Methods. Finally, we spatially normalized the raw fluorescence trace (Online Methods equation (4)) before visualization (**Fig. 3f**). Although the jumps along the *z* direction took the same time as the steps in the point-by-point scanning mode, by increasing the sampling rate of the detectors we recorded with approximately tenfold higher spatial sampling rate during lateral drifting as compared to point-by-point scanning (595.2 points per kHz instead of 54.3 points per kHz). The PSF did not change during the lateral drift (**Fig. 3g, Supplementary Fig. 1d** and **Supplementary Note 8**). The sequence of fast drifts in the *x-y* direction and jumps in the *z* direction allowed us to perform high-speed sampling with high spatial discretization along 3D trajectories.

High-speed *in vivo* 3D imaging of neuronal network activity
To test the performance of our imaging system *in vivo*, we recorded Ca²⁺ responses from a population of individual neurons in the visual cortex of adult anesthetized mice. We injected a mixture of Oregon Green 488 BAPTA-1 acetyloxy methyl ester (OGB-1–AM) to monitor changes in intracellular Ca²⁺ concentrations and

sulforhodamine-101 (SR-101)[30] to selectively label glial cells (**Fig. 4a**). Red fluorescence of SR-101 allowed differentiation between neurons and glial cells (**Fig. 4b,c** and **Supplementary Fig. 11**). The maximal power of our laser (3.5 W) limited the depth of the *in vivo* recording to a maximum of 500 μm from the surface of the cortex (total imaging volume was 400 μm × 400 μm × 500 μm *x*, *y* and *z*, respectively). Once we identified a region with well-stained cells (**Fig. 4c**), we selected a reference cell (a brightly red-fluorescing glial cell), scanned it in three dimensions and defined the 3D origin ((0, 0, 0) coordinate) of our recording as the center of this glial cell (**Fig. 4d**). To compensate for tissue drift, we rescanned the 'origin-glia' cell and repositioned the center of the origin glia to the (0, 0, 0) coordinate by moving the table and the objective (Online Methods). We automated this tissue-drift compensation and performed it plane by plane when obtaining a reference *z* stack or between 3D random-access scans. Next, we recorded a reference *z* stack and, using an automated algorithm, identified the neuron and glial cell bodies (**Supplementary Note 9**). The algorithm listed the 3D coordinates of the centers of each neuronal cell body and this coordinate was used for random-access activity imaging (**Fig. 4d**–**f**, **Supplementary Fig. 11b** and Online Methods). Cells included in the scanning could also be added or removed manually either by scrolling up and down through the *z* stack in two dimensions[2] or by using the 3D interactive virtual environment (**Supplementary Video 2** and **Supplementary Note 5**).

After the selection of the cell bodies, we recorded the spontaneous activity of each neuron by scanning at 56 Hz and plotted the recorded raw and point-by-point background-corrected and normalized fluorescence data in real time, each row showing the activity of a single cell (**Fig. 4g**). We monitored the stability of long-term recording using the baseline fluorescence. In the recording session depicted in **Figure 4g**, 532 neurons displayed spontaneous Ca²⁺ transients. We found some evidence of
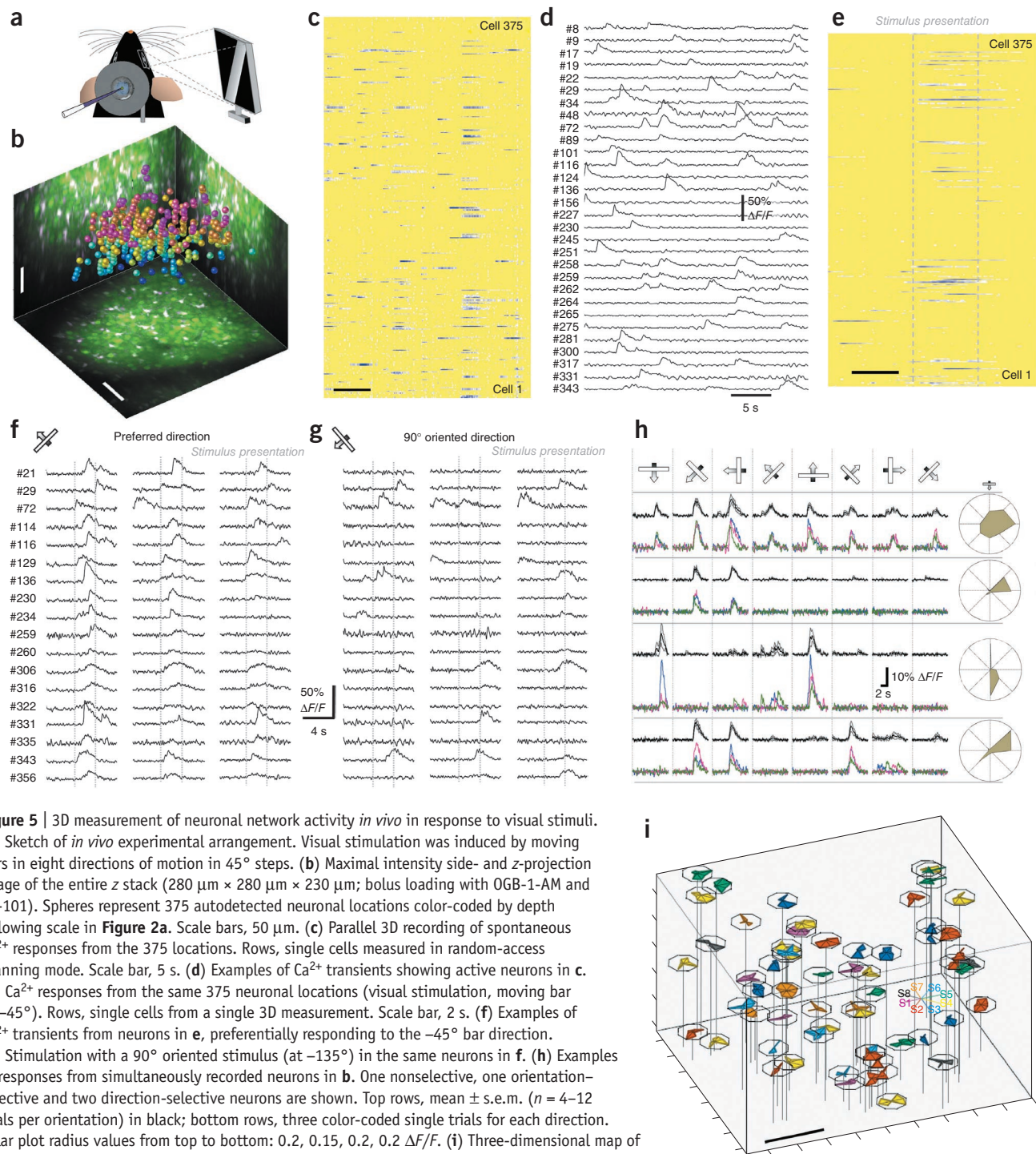
Figure 5 | 3D measurement of neuronal network activity *in vivo* in response to visual stimuli. (**a**) Sketch of *in vivo* experimental arrangement. Visual stimulation was induced by moving bars in eight directions of motion in 45° steps. (**b**) Maximal intensity side- and *z*-projection image of the entire *z* stack (280 μm × 280 μm × 230 μm; bolus loading with OGB-1-AM and SR-101). Spheres represent 375 autodetected neuronal locations color-coded by depth following scale in **Figure 2a**. Scale bars, 50 μm. (**c**) Parallel 3D recording of spontaneous Ca²⁺ responses from the 375 locations. Rows, single cells measured in random-access scanning mode. Scale bar, 5 s. (**d**) Examples of Ca²⁺ transients showing active neurons in **c**. (**e**) Ca²⁺ responses from the same 375 neuronal locations (visual stimulation, moving bar at −45°). Rows, single cells from a single 3D measurement. Scale bar, 2 s. (**f**) Examples of Ca²⁺ transients from neurons in **e**, preferentially responding to the −45° bar direction. (**g**) Stimulation with a 90° oriented stimulus (at −135°) in the same neurons in **f**. (**h**) Examples of responses from simultaneously recorded neurons in **b**. One nonselective, one orientation–selective and two direction-selective neurons are shown. Top rows, mean ± s.e.m. (*n* = 4–12 trials per orientation) in black; bottom rows, three color-coded single trials for each direction. Polar plot radius values from top to bottom: 0.2, 0.15, 0.2, 0.2 *ΔF/F*. (**i**) Three-dimensional map of orientation- and direction-selective cells measured in three dimensions in the volume in **b**. Scale bar, 40 μm.

synchronized spontaneous activity among the neurons imaged, but asynchronous spontaneous activity was more frequent in these mice (*n* = 15; **Fig. 5a–d**).

Next, we presented the mouse with visual stimuli consisting of movies of a white bar oriented at eight different angles and moving in a direction always perpendicular to its orientation (**Fig. 5a** and **Supplementary Protocol 2**). We show an example of visually evoked responses from 375 neurons recorded 80 times per second (**Fig. 5b,e–i**). Visual stimulation with bars oriented at −45° to vertical, activated a small subpopulation

of the measured cells (**Fig. 5e**). Note the repeatability of the responses during movie presentations at successive stimulations in the selected cells (**Fig. 5f**). An orthogonally moving bar, at −135°, activated fewer cells from the same cell population and induced a different response pattern (**Fig. 5g**). In general, the group of cells from the total imaged population that preferentially responded to the 90°-oriented stimulation was different from that responding to the −45° orientation (**Fig. 5f,g** and see **Supplementary Fig. 12a,b** for the response pattern of the cells preferring the −135° stimulus). We then compared the

responses of the 375 individual cells to bars moving in eight different directions (we recorded 28,125 Ca^{2+} transients) and found orientation-selective, direction-selective and orientation-nonselective cells in the full neuronal population measured simultaneously in three dimensions (**Fig. 5h,i** and **Supplementary Fig. 12c**). To show orientation tuning independent of the receptive field location, we repeated our 3D-scanning measurements in 307 neurons located in a z-scanning range of >600 µm and stimulated the mice with moving gratings (**Supplementary Fig. 13** and **Supplementary Results 3**).

DISCUSSION

Despite the impressive progress in live microscopy in recent years[2,7,13,16,17,25], noninvasive recording of neuronal activity with satisfactory spatial and temporal resolution as well as acquisition data rate, from long neuronal processes of individual cells or from hundreds of cell bodies in neuronal populations, has remained a challenge both *in vitro* and *in vivo*. Our 3D-imaging two-photon microscope can be used to scan a large scanning volume (up to 700 µm × 700 µm × 1,400 µm), with a scanning speed of up to 54.3 points per kHz (>500 points per kHz in 3D trajectory scanning mode), with 470 nm × 490 nm × 2,490 nm resolution in the center core and less than 1.9 µm × 1.9 µm × 7.9 µm resolution throughout the entire scanning volume (**Supplementary Discussion 1**). The microscope-associated software performed online data analysis, 3D interactive visualization and accelerated selection of regions of interest.

The improved performance of our microscope can be explained by several factors. Detailed, diffraction-based optical modeling predicted an optimal arrangement of passive and active optical elements that were selected from a number of combinations. Modeling helped optimize angular dispersion compensation. In contrast to previous arrangements, we neither grouped the four AO deflectors in the most compact arrangement[19] nor separated them with relay lenses[15]. Rather, we grouped them into two functionally different subunits to increase the lateral field of view of scanning. Random-access positioning in the x-y plane was restricted only to the second group of deflectors (2D-AO scanning unit). In addition, not only deflector driver signals, but also deflector geometry, manufacturing, bandwidth and TeO_2 orientation differ between deflectors of the two groups (**Supplementary Discussion 1**). In contrast to previous realizations of AO scanning[15,17,19,24], we dynamically compensated for optical errors (astigmatism, field curvature, angular dispersion and chromatic aberration) during measurements by adding corrections to the AO deflector driver functions at each imaged point before starting the measurement: this increased spatial resolution in the whole scanning volume. Dynamic optical compensation also allowed compensation for focal-spot displacement (and optical errors) at a wide range of laser light wavelengths. The field of view increased owing to the separation of the deflectors into two groups and the use of the properly illuminated large aperture objectives. In contrast, spatial resolution increased as a consequence of properly selected AO deflectors and system aperture, angular dispersion and dynamic optical error compensation.

With this setup, simultaneous two-photon imaging and optogenetic perturbation, or two-photon imaging combined with two-photon uncaging[2,3,31] may become possible in three dimensions in the future.

METHODS

Methods and any associated references are available in the online version of the paper at http://www.nature.com/naturemethods/.

Note: Supplementary information is available on the Nature Methods website.

AUTHOR CONTRIBUTIONS
Optical design was performed by P.M., G.S. and M.V. Software was written by G.K. *In vitro* measurements were performed by B.C., A.K., G.S. and Ba.R. *In vivo* measurements were designed by D.H. and performed by D.H., A.K., G.S. and Ba.R. Analysis was carried out by Ba.R., A.K., G.K. and G.S. This manuscript was written by Ba.R., Bo.R., D.H., G.K., A.K. and P.M., with comments from all authors. Ba.R., Bo.R., E.S.V. and P.M. supervised the project.

COMPETING FINANCIAL INTERESTS
The authors declare competing financial interests: details accompany the full-text HTML version of the paper at http://www.nature.com/naturemethods/.

Published online at http://www.nature.com/naturemethods/.
Reprints and permissions information is available online at http://www.nature.com/reprints/index.html.

1. Johnston, D. & Narayanan, R. Active dendrites: colorful wings of the mysterious butterflies. *Trends Neurosci.* **31**, 309–316 (2008).
2. Katona, G. *et al.* Roller Coaster Scanning reveals spontaneous triggering of dendritic spikes in CA1 interneurons. *Proc. Natl. Acad. Sci. USA* **108**, 2148–2153 (2011).
3. Losonczy, A., Makara, J.K. & Magee, J.C. Compartmentalized dendritic plasticity and input feature storage in neurons. *Nature* **452**, 436–441 (2008).
4. Spruston, N. Pyramidal neurons: dendritic structure and synaptic integration. *Nat. Rev. Neurosci.* **9**, 206–221 (2008).
5. Rozsa, B., Katona, G., Kaszas, A., Szipocs, R. & Vizi, E.S. Dendritic nicotinic receptors modulate backpropagating action potentials and long-term plasticity of interneurons. *Eur. J. Neurosci.* **27**, 364–377 (2008).
6. Rozsa, B., Zelles, T., Vizi, E.S. & Lendvai, B. Distance-dependent scaling of calcium transients evoked by backpropagating spikes and synaptic activity in dendrites of hippocampal interneurons. *J. Neurosci.* **24**, 661–670 (2004).
7. Ohki, K., Chung, S., Ch'ng, Y.H., Kara, P. & Reid, R.C. Functional imaging with cellular resolution reveals precise micro-architecture in visual cortex. *Nature* **433**, 597–603 (2005).
8. Ariav, G., Polsky, A. & Schiller, J. Submillisecond precision of the input-output transformation function mediated by fast sodium dendritic spikes in basal dendrites of CA1 pyramidal neurons. *J. Neurosci.* **23**, 7750–7758 (2003).
9. Cheng, A., Goncalves, J.T., Golshani, P., Arisaka, K. & Portera-Cailliau, C. Simultaneous two-photon calcium imaging at different depths with spatiotemporal multiplexing. *Nat. Methods* **8**, 139–142 (2011).
10. Durst, M.E., Zhu, G. & Xu, C. Simultaneous spatial and temporal focusing for axial scanning. *Opt. Express* **14**, 12243–12254 (2006).
11. Holekamp, T.F., Turaga, D. & Holy, T.E. Fast three-dimensional fluorescence imaging of activity in neural populations by objective-coupled planar illumination microscopy. *Neuron* **57**, 661–672 (2008).
12. Nikolenko, V. *et al.* SLM microscopy: scanless two-photon imaging and photostimulation with spatial light modulators. *Front Neural Circuits* **2**, 5 (2008).
13. Gobel, W., Kampa, B.M. & Helmchen, F. Imaging cellular network dynamics in three dimensions using fast 3D laser scanning. *Nat. Methods* **4**, 73–79 (2007).
14. Kaplan, A., Friedman, N. & Davidson, N. Acousto-optic lens with very fast focus scanning. *Opt. Lett.* **26**, 1078–1080 (2001).
15. Duemani Reddy, G., Kelleher, K., Fink, R. & Saggau, P. Three-dimensional random access multiphoton microscopy for functional imaging of neuronal activity. *Nat. Neurosci.* **11**, 713–720 (2008).

16. Grewe, B.F. & Helmchen, F. Optical probing of neuronal ensemble activity. *Curr. Opin. Neurobiol.* **19**, 520–529 (2009).
17. Grewe, B.F., Langer, D., Kasper, H., Kampa, B.M. & Helmchen, F. High-speed *in vivo* calcium imaging reveals neuronal network activity with near-millisecond precision. *Nat. Methods* **7**, 399–405 (2010).
18. Iyer, V., Hoogland, T.M. & Saggau, P. Fast functional imaging of single neurons using random-access multiphoton (RAMP) microscopy. *J. Neurophysiol.* **95**, 535–545 (2006).
19. Kirkby, P.A., Srinivas Nadella, K.M. & Silver, R.A. A compact acousto-optic lens for 2D and 3D femtosecond based 2-photon microscopy. *Opt. Express* **18**, 13721–13745 (2010).
20. Otsu, Y. *et al.* Optical monitoring of neuronal activity at high frame rate with a digital random-access multiphoton (RAMP) microscope. *J. Neurosci. Methods* **173**, 259–270 (2008).
21. Reddy, G.D. & Saggau, P. Fast three-dimensional laser scanning scheme using acousto-optic deflectors. *J. Biomed. Opt.* **10**, 064038 (2005).
22. Rozsa, B. *et al.* Random access three-dimensional two-photon microscopy. *Appl. Opt.* **46**, 1860–1865 (2007).
23. Salome, R. *et al.* Ultrafast random-access scanning in two-photon microscopy using acousto-optic deflectors. *J. Neurosci. Methods* **154**, 161–174 (2006).
24. Vucinic, D. & Sejnowski, T.J. A compact multiphoton 3D imaging system for recording fast neuronal activity. *PLoS ONE* **2**, e699 (2007).
25. Stosiek, C., Garaschuk, O., Holthoff, K. & Konnerth, A. In vivo two-photon calcium imaging of neuronal networks. *Proc. Natl. Acad. Sci. USA* **100**, 7319–7324 (2003).
26. Jia, H., Rochefort, N.L., Chen, X. & Konnerth, A. Dendritic organization of sensory input to cortical neurons *in vivo*. *Nature* **464**, 1307–1312 (2010).
27. Polsky, A., Mel, B.W. & Schiller, J. Computational subunits in thin dendrites of pyramidal cells. *Nat. Neurosci.* **7**, 621–627 (2004).
28. Agoston, A. Equivalent time pseudorandom sampling system. *Patent* US 4678345 (1987).
29. Christie, J.M., Chiu, D.N. & Jahr, C.E. Ca(2+)-dependent enhancement of release by subthreshold somatic depolarization. *Nat. Neurosci.* **14**, 62–68 (2011).
30. Nimmerjahn, A., Kirchhoff, F., Kerr, J.N. & Helmchen, F. Sulforhodamine 101 as a specific marker of astroglia in the neocortex *in vivo*. *Nat. Methods* **1**, 31–37 (2004).
31. Matsuzaki, M. *et al.* Dendritic spine geometry is critical for AMPA receptor expression in hippocampal CA1 pyramidal neurons. *Nat. Neurosci.* **4**, 1086–1092 (2001).

ONLINE METHODS

Optical engineering. Details on optical engineering are provided in **Supplementary Note 1**.

The 3D-imaging microscope design. We modeled the optical design of the microscope using OSLO (Lambda Research) and ZEMAX (ZEMAX Development) optical designer programs. Several parameters of the optical system were optimized using built-in and custom optimization algorithms written in MATLAB (MathWorks) and Mathcad (Mathsoft; **Supplementary Software 1**). Following the arrangement suggested by the model (**Supplementary Note 1**), a large aperture (15–17 mm) optical assembly was constructed (**Fig. 1a**). Here a Ti:S laser with automated dispersion compensation provides the laser pulses. A Faraday isolator blocks the coherent backreflections. A four-prism sequence[32] adds a large negative second- and third-order dispersion ($-72,000$ fs^2 and $-40,000$ fs^3) to precompensate for pulse broadening caused by the optical elements of the system (dispersion compensation unit, **Fig. 1a,e** and **Supplementary Note 4**). An automated beam stabilization unit is necessary to stabilize precise alignment of the long beam path and cancel out subtle thermal-drift errors. This is built from position sensors (quadrant detectors) and motorized mirrors, wired in a feedback loop. The beam is then magnified by a beam expander to match the large apertures (15 mm) of the first pair of AO deflectors. These deflectors form two orthogonal electric cylinder lenses filled with continuously changing frequency ('chirped') acoustic waves[14], and are used for z focusing (AO z-focusing unit). Next, laser beams from the x and y cylindrical lenses are projected to the x and y AO deflectors (17 mm apertures) of the 2D scanning unit, respectively, by telecentric projection. This 2D-AO scanning unit performs lateral scanning and also compensates for the lateral drift of the focal spot generated by the cylindrical lenses during z focusing[14] (drift compensation). The angular dispersion compensation unit optically links the 2D-AO scanning unit with the objective. Modeling helped us to design and manufacture a custom-made lens made of high dispersion glass with aspheric and conic surfaces (**Supplementary Note 2** equations 13 and 14), which, combined with a telecentric projection of the AO scanner unit to the objective's back aperture, diminishes the angular dispersion introduced by the AO devices at off-axis positions ($x,y \neq 0$). Then, the 3D scanning system is coupled to a 2D two-photon microscope in which fluorescent signals are collected by photomultiplier tubes fixed directly onto the objective arm for high photon-collection efficiency. Finally, an interactive 3D virtual environment based on a 3D display system and a 3D mouse provides direct, accelerated interaction between the user and the 3D space of the sample (**Supplementary Videos 1** and **2** and **Supplementary Note 5**).

The optical pathway was realized according to the modeling. Laser pulses were provided by a Mai Tai DeepSee femtosecond laser (800–850 nm, 3.5 W maximum, SpectraPhysics). Pulse backreflection to the laser source was eliminated by a Faraday isolator (BB8-5I, Electro-Optics Technology). Next beam position was stabilized using two motorized mirrors (**Fig. 1a**; AG-M100N, Newport), which stabilized the position of the light transmitted by two backside custom-polished broad-band mirrors (BB2-E03; Thorlabs) on the surface of two quadrant detectors (**Fig. 1a**; PDQ80A, Thorlabs). The positioning feedback loop

(U12, LabJack Corporation) was controlled by a program written in LabView (National Instruments). The beam was expanded by two achromatic lenses arranged in a Galilean telescope (focal length (f) = -75 mm, ACN254-075-B, Thorlabs; f = 200 mm, NT47319, Edmund Optics; distance = 125.62 mm) to match the large apertures of the first pair of AO deflectors (15 mm). Mirrors, $\lambda/2$ waveplates and holders, were purchased from Thorlabs and Newport. AO deflectors have been custom designed and manufactured at Budapest University of Technology and Economics (**Supplementary Note 3**). Achromatic telecentric relay lenses were purchased from Edmund Optics (f_{TC} = 150 mm, NT32-886). Achromatic scan and tube lenses were chosen from Edmund Optics (f = 250 mm, NT45-180) and Olympus (f = 210 mm), respectively. The AO-based 3D scanner system was attached to the top of a galvanometer-based upright two-photon microscope (Femto2D-Alba, Femtonics Ltd.) using custom-designed rails. AO sweeps were generated by the direct digital synthesizer chips (AD9910, 1 GSPS, 14-bit, Analog Devices) which were integrated into the microscope's modular electronic system using FPGA elements (Xilinx; **Supplementary Software 1**). Red and green fluorescence was separated by a dichroic filter (39 mm, 700dcxru, Chroma Technology) and was collected by GaAsP photomultiplier tubes custom-modified for high collection efficiency of scattered photons (PMT, H7422P-40-MOD, Hamamatsu), fixed directly onto the objective arm. In *in vitro* experiments the forward emitted fluorescence was also collected by 2-inch aperture detectors positioned below the condenser lens (Femto2D-Alba, Femtonics). Signals of the same wavelength measured at the epi- and *trans*fluorescent positions have been totaled. All measurements except otherwise noted were carried out using the large aperture XLUMPlanFI20x/0.95 (Olympus, 20×, NA 0.95) objective. For comparison the large-aperture CFI75 LWD 16XW (Nikon, 16×, NA 0.8) and the small aperture LUMPlanFI/IR 60× (Olympus, 60×, NA 0.8) were also tested. Maximal output laser power in front of the objective is 320 mW.

The optical performance (spatial and temporal resolution) of the microscope was also tested on nonliving samples (**Supplementary Results 1**, **Supplementary Figs. 1**–**7** and **14**, **Supplementary Protocol 3**).

AO deflectors and drivers. One difference between the system described here and previous designs is that the AO deflectors form functionally and physically different groups (**Supplementary Note 3**). The first AO pair is used for z focusing, whereas lateral scanning is performed entirely by the second pair (2D AO scanning unit). This arrangement increased the diameter of the lateral scanning range by a factor of ~2.7 (**Fig. 1b** and **Supplementary Fig. 2a,b**). Furthermore, not only electronic driver function, but also deflector geometry, TeO_2 crystal orientation and bandwidth are different between deflectors of the z focusing and the 2D AO scanning unit (**Supplementary Note 3**). Altogether these factors increased the diameter of the lateral scanning range up to 720 µm (**Fig. 1b** and **Supplementary Fig. 2a**). Design, manufacturing and property of AO deflectors are described in **Supplementary Note 3**.

Angular dispersion compensation unit. In contrast to previous AO microscope designs, we also took advantage of the active optical elements to compensate for optical errors (astigmatism, field curvature, angular dispersion and chromatic aberration)

dynamically, which increased spatial resolution especially during AO z focusing (at $z \neq 0$ planes by a factor of ~2–3; **Fig. 1c,d** and **Supplementary Fig. 3c**). The optimal compensation parameters were determined for each point of the scanning volume in advance and loaded into the driver electronics accordingly. Spatial resolution in the whole scanning volume is also increased by the large optical apertures used throughout the system, and ~20% of this increase was due solely to the use of large AO deflector apertures (**Fig. 1b–d**, **Supplementary Fig. 2c** and **Supplementary Note 3**). In contrast to the dominantly z-focusing–dependent effect of dynamic error compensation, the angular dispersion compensation unit decreased the PSF in off-axis positions when compared with a simple two-lens telecentric projection (**Fig. 1c** and **Supplementary Fig. 3d,e**). These factors, which decrease PSF, inherently increase the lateral field of view (**Fig. 1b**). The spatially variable angular dispersion introduced by the acousto-optic scanner was compensated by a lens array containing a custom-made lens made of high dispersion glass with aspheric and conic surfaces (**Supplementary Note 2**).

Material dispersion compensation. Here we needed to compensate for about 72,000 fs^2 second-order dispersion and about 40,000 fs^3 third-order dispersion; the precise amount depended on the objective used and on the central wavelength. We added a two-pass four-prism compressor (Proctor & Wise)[22,32] that provided a fixed compensation amount at a given wavelength. This was combined with the variable compensation provided by the DeepSee unit of the MaiTai laser to allow dynamic adjustable dispersion compensation for optimum fluorescence signal (**Supplementary Note 4**).

Continuous 3D trajectory scanning with AO deflectors. A new design aspect of the scanning method applied here is the active use of a lateral drift error in AO z focusing to perform 3D trajectory scanning. This continuous drift was used to measure activity in long cellular processes. When the optical aperture of the x or y electrical cylindrical lenses of the z-focusing unit is filled with chirped acoustic waves, the various portions of the optical beam are deflected in different directions. Thus, depending on the slope of the frequency, focusing to a given plane can be maintained until the frequency of the chirped acoustic waves reaches the band limit of the crystals. An 'unwanted' effect of the chirp is that the mean acoustic frequency in the AO device also changes, resulting in a continuous change in the lateral deflection of the beam and, thus, generating lateral drift of the focal spot. In previous designs, this lateral drift was completely compensated and eliminated during random-access AO scanning by adding a second AO deflector with counter-propagating chirped acoustic waves[14,15,19]. However, partial compensation by the counter-propagating chirped AO waves (added to the driving signal of the 2D AO scanning unit deflectors) can generate fast lateral movements of the focal spot in preferred directions, with defined speed at a given z focus (continuous 3D trajectory scanning mode). This lateral movement was used to scan continuously, with z-jump interruptions, along the 3D trajectory of a dendrite with a spatial sampling rate up to two orders of magnitude higher (higher spatial discretization) than in 3D random-access scanning.

Here we describe how a partial compensation of a chirped acoustic wave with a counter-propagating differently chirped acoustic wave can result in continuous line-scanning with a given velocity in a given focal plane when the frequency slopes of the chirps of the focusing and counter-propagating AO waves are selected properly (**Fig. 3f**).

Briefly, the temporal variation of the deflected beam angle of the laser beam emerging from one AO deflector with an acoustic sweep of slope a is described by the acousto-optic law[14]

$$\frac{\partial \alpha}{\partial t} = K \times \frac{\partial \omega}{\partial t} = K \times a \qquad (1)$$

where K describes the dependence of the deflection angle α on the acoustic frequency ω in a given deflector $\alpha = K \times \omega$, and t is time. When this AO deflector is combined with a second AO deflector with counter-propagating chirped acoustic pulses, the subsequent optics with magnification M and the objective with effective focal length f_{obj} transform this angle variation into the lateral shift of the spot in the focal plane with velocity

$$v = \left(K_2 a_2 - K_1 a_1 \right) \times \frac{f_{obj}}{M} \qquad (2)$$

where a_1 and a_2 are the chirps of the focusing and the counter-propagating AO waves, in the first and second AO deflector, respectively, and K is different for the first (K_1) and second deflectors (K_2) because they have different configurations and geometries. The movement of the focal spot is restricted to a given z plane if the slopes in a deflector pair are shifted symmetrically to maintain

$$K_2 a_2 + K_1 a_1 = \text{constant} \qquad (3)$$

Our optical model determined the chirp parameters required, and these were confirmed in measurements on fluorescent beads (**Fig. 3g**).

The same is valid for both x and y cylindrical lenses. Thus, continuous scanning in any arbitrary direction with a given speed can be realized with small jumps along the z axis (continuous 3D trajectory scanning), or the velocity can be set to zero, thus realizing a random-access scanning mode.

We use a fairly simple method in the algorithm that determines the frequency sweep slopes, which cause the spot to move in a plane at a prescribed z depth in the required direction with a prescribed velocity v (**Supplementary Note 7** equations 25,26).

Our simulations and measurements have also shown that the spatial resolution does not change noticeably during the drift (**Fig. 3g**, **Supplementary Fig. 1d** and **Supplementary Note 8**).

Selected guide points along the length of a dendrite were homogeneously resampled by using piecewise cubic Hermite interpolation (implemented in the MATLAB's pchip function http://www.mathworks.in/help/techdoc/ref/pchip.html). This algorithm was chosen over the conventional spline interpolation because it never overshoots the guide points.

Random equivalent-time sampling mode for 3D measurements. The reconstruction of the mean time course of transients is also possible by adopting a random equivalent-time sampling mode from oscilloscope technology[28] for 3D fluorescence measurements. Namely, in random-access fluorescence measurements the recording system acquires samples while sequentially jumping through a predefined set of 3D locations, sampling the same location with a defined frequency (sampling rate). One way of determining the

mean signal at a given location is simply by averaging each trial using the trigger signal of the optical recording start time. Another way is to use the time of the peak of the somatic action potential as time zero (action potential trigger). When the action potential–triggered average of transients is calculated, each trial is shifted 'randomly' relative to the others on a very fine time scale due to the biological variability of the trigger (**Supplementary Fig. 10**). Therefore, samples in successive trials are added into equally distributed sub-intervals of the sampling time (**Supplementary Fig. 10a,c**). By plotting the mean ± s.e.m. values of the samples gathered in the sub-intervals as a function of time, the mean waveform of the event can be reconstructed with a higher temporal resolution than that dictated by the sampling rate (74.4 kHz instead of 7.44 kHz, **Supplementary Fig. 10c,d**). Note that if the jitter of the biological signal (here that of the action potentials) is not enough to generate an efficient random trigger, Ca^{2+} measurements can be started randomly to yield a similar result.

Animals. Male or female C57Bl/6J wild-type mice or Wistar rats were kept under a 12-h day and night cycle with food and water provided ad libitum and were handled in accordance with the Hungarian Act of Animal Care and Experimentation (1998; XXVIII, section 243/1998.). The Animal Care and Experimentation Committee of the Institute of Experimental Medicine of the Hungarian Academy of Sciences and the Animal Health and Food Control Station, Budapest, has approved the experimental design (reference numbers 22.1/4015/003/2009, 18_1/2009 and 19_1/2009).

Slice preparation and electrophysiology. Acute hippocampal slices were prepared from Wistar rats (postnatal ages 16–20 d) or C57Bl6/J (postnatal ages 16–26 d) mice using isoflurane anesthesia followed by swift decapitation. Horizontal (300–400 μm) brain slices were cut with a vibratome and stored at room temperature (23 °C) in artificial cerebrospinal fluid (ACSF) (126 mM NaCl, 2.5 mM KCl, 2 mM $CaCl_2$, 2 mM $MgCl_2$, 1.25 mM NaH_2PO_4, 26 mM $NaHCO_3$ and 10 mM glucose) as previously described[2,5,6].

Hippocampal CA1 pyramidal cells were visualized using 900 nm infrared lateral illumination[5]. Current-clamp recordings were made at 23 °C and 33 °C (MultiClamp 700B, Digidata 1440: Molecular Devices; chamber heater: Luigs & Neumann; in-line heater: Supertech). For whole-cell current-clamp recordings, glass electrodes (6–9 MΩ) were filled with 125 mM K-gluconate, 20 mM KCl, 10 mM HEPES, 10 mM di-Tris-salt phosphocreatine, 0.3 mM Na-GTP, 4 mM Mg-ATP, 10 mM NaCl and 0.1 mM Oregon Green BAPTA-1 (OGB-1, Invitrogen). In propagation speed measurements, 0.2 mM Fluo-5F pentapotassium salt (Invitrogen) and 0.04 mM Alexa Fluor 594 (Invitrogen) were used instead of OGB-1. For extracellular current-clamp recordings, glass electrodes (6–9 MΩ) were filled with ACSF or with ACSF containing 1 M NaCl. All chemicals and drugs, unless otherwise noted, were purchased from Sigma. Cells with a resting membrane potential more negative than −50 mV were accepted.

Focal synaptic stimulation was performed as described previously[2,5,6] (**Supplementary Protocol 1**). Two-photon imaging started 15–20 min after attaining the whole-cell configuration.

The 3D virtual-reality user interface. The 3D user interface and visualization method are provided in **Supplementary Note 5** and in **Supplementary Software 2**.

Automatic drift compensation algorithm. Once a region with well-stained cells had been identified (**Fig. 4c**), we selected a reference cell (preferably a brightly red-fluorescing glial cell) and scanned it in three dimensions. We defined the 3D origin ((0, 0, 0) coordinate) of our recording as the center of this glial cell (**Fig. 4d**). To compensate for tissue drift, we rescanned the 'origin-glia' cell and, using profiles of the scan, localized its center. We repositioned the center of the origin-glia to the (0, 0, 0) coordinate by moving the motorized shifting table and the objective; this way all cells were shifted back to the (microscope-fixed) 3D location where they were selected for measurement. This tissue drift compensation was automated and performed plane by plane when obtaining a reference z stack or between 3D random-access scans. See **Supplementary Software 3** for details.

Detection of fluorescently labeled cells. The cell-detection algorithm was developed to quickly find and select the cell body centers in large neuronal ensembles during the measurement. See **Supplementary Note 9** and **Supplementary Software 4**.

In vivo bolus loading. Male or female C57Bl/6J wild-type mice (postnatal age 60–130 d) were used. The procedure for surgery and in vivo bolus loading was performed as previously described[25]. Briefly, mice were sedated with isoflurane and anesthetized with an intraperitoneal injection of chlorprothixene (0.05 mg kg^{-1}) and urethane (0.75 mg kg^{-1}). The skull was exposed and a cranial window (3 mm diameter) was opened above the visual cortex (V1). Bulk loading was performed with a patch pipette using Oregon Green BAPTA-1 AM (2 mM, Invitrogen) and sulforhodamine-101 (200 μM, Invitrogen) under two-photon guidance (810 nm), and a cover glass was fixed to the skull above the cranial window, along with a light-shielding cone. Cell imaging was started 1 h after dye loading to allow for proper staining.

Visual stimulation. The visual stimulation protocol is given in **Supplementary Protocol 2**.

Data analysis and statistics. Measurement control, real-time data acquisition and analysis were performed with a MATLAB-based program (MES, Femtonics) and by custom-written software. The spatially normalized and projected Ca^{2+} response (defined as the 3D Ca^{2+} response) was calculated from the raw 3D line-scan data, $F(d,t)$ by applying the

$$\Delta F / F = (F(d,t) - F_0(d)) / F_0(d) \qquad (4)$$

formula, where t denotes time and d denotes distance along the curve or the ordinal number of a given point in a random-access scanning series. $F_0(d)$ denotes the average background-corrected pre-stimulus fluorescence as a function of d. All 3D Ca^{2+} responses are color-coded (colors from yellow to blue show increasing Ca^{2+} responses), and projected as a function of d and t. Electrophysiological data were acquired using either pClamp8 or pClamp10 (Molecular Devices) and MES (Femtonics) software. Statistical comparisons were performed using Student's paired t-test. Unless otherwise indicated, data are presented as means ± s.e.m.

32. Proctor, B. & Wise, F. Quartz prism sequence for reduction of cubic phase in a mode-locked Ti:Al(2)O(3) laser. *Opt. Lett.* **17**, 1295–1297 (1992).